Nanoscale

Synthesis of Lead-free $Cs_3Sb_2Br_9$ Perovskite Alternative Nanocrystals with Enhanced Photocatalytic CO_2 Reduction Activity

Journal:	*Nanoscale*
Manuscript ID	NR-COM-09-2019-007722.R1
Article Type:	Communication
Date Submitted by the Author:	11-Jan-2020

Complete List of Authors:	Lu, Chang; Wake Forest University Itanze, Dominique; Wake Forest University, Chemistry Aragon, Alexander; Wake Forest University, Chemistry Ma, Xiao; Wake Forest University, Chemistry Li, Hui; Wake Forest University Ucer, Kamil; Wake Forest University, Physics Hewitt, Corey; Wake Forest University, Center for Nanotechnology and Molecular Materials Carroll, Dave; Wake Forest University, Physics Williams, Richard; Wake Forest University, Physics Qiu, Yejun; Harbin Institute of Technology, Materials Science and Engineering Geyer, Scott; Wake Forest University

COMMUNICATION

Synthesis of Lead-free $Cs_3Sb_2Br_9$ Perovskite Alternative Nanocrystals with Enhanced Photocatalytic CO_2 Reduction Activity

Received 00th January 20xx,
Accepted 00th January 20xx

DOI: 10.1039/x0xx00000x

Chang Lu[a], Dominique S. Itanze[a], Alexander G. Aragon[a], Xiao Ma[a], Hui Li[a], Kamil B. Ucer[b], Corey Hewitt[b,c], David L. Carroll[b,c], Richard T. Williams[b], Yejun Qiu[d], Scott Geyer[a,*]

A synthetic method for uniform and pure $Cs_3Sb_2Br_9$ NCs has been developed. $Cs_3Sb_2Br_9$ NCs exhibit a 10-fold increase in activity for the photocatalytic CO_2 reduction reaction compared to $CsPbBr_3$ NCs, achieving 510 µmol CO/g cat. after 4 h. Density functional theory shows that $Cs_3Sb_2Br_9$ surfaces sufficiently expose Sb to allow reactivity, as opposed to the unreactive $CsPbBr_3$ surface.

The unique optical properties of Pb-based halide perovskite nanocrystals (NCs)[1] have led to their application as the active layer for light harvesting[2,3] and light emitting applications[4–7]. However, the incorporation of toxic Pb in the crystal structure poses a challenge for commercialization and therefore the development for Pb-free halide perovskite materials is highly desired. In recent years, a series of colloidal Pb-free NCs have been studied, such as $CsSnX_3$[8,9] and double perovskite Cs_2AgBiX_6[10–14]. However, stability remains a challenge for these materials. For this reason, Pb-free perovskite structures such as $Cs_3Sb_2X_9$[15,16] and $Cs_3Bi_2X_9$[17–19] are seen as promising materials that maintain key aspects of the perovskite system but exhibit better thermal stability.

As strong light absorbers with a band gap that is tunable in the visible region by altering the halide composition, halide perovskites are of interest for photocatalysis. In particular, photocatalysts[20–25] capable of converting CO_2 to fuels and feedstocks (CO, CH_4, CH_3OH, etc.) directly from visible solar energy are highly sought after. While halide perovskite materials are excellent light absorbers, to date the application for photocatalytic reactions is relatively rare, which can be partially attributed to the stability issues of many of these compounds. Recently, Xu et al. applied $CsPbBr_3$ NCs/graphene oxide composite[26] and Hou et al reported pure $CsPbBr_3$ NCs[27] as a catalyst for solar-driven CO_2 reduction reaction (CO_2RR), with modest efficiencies of 20-30 µmol(CO)/g cat. yield. Later, Zhou et al.[10] prepared Pb-free Cs_2AgBiX_6 NCs for CO_2RR with similar production as the Pb-based counterparts (15 µmol(CO)/g cat.). While Ou et al[28] developed a system that anchors $CsPbBr_3$ NCs on g-C_3N_4 which achieved a higher yield of 149 µmol CO h^{-1} g^{-1}, the NCs in this structure are primarily acting as photo-absorbers while g-C_3N_4 is acting as the catalytic interface. For comparison, the most common oxide perovskite CO_2 reduction catalyst is $SrTiO_3$[29] which produces over 352 µmol CO h^{-1} g^{-1} under ultra-violet (UV) illumination. However, $SrTiO_3$, while robust, is fundamentally limited by the large bandgap that absorbs only UV light, limiting the spectral efficiency.

From a catalytic perspective, the lead-free alternatives allow the application of different metal centers (e.g. Sb, Bi) which may have higher catalytic activity and better selectivity. In this letter, we adapted the hot injection method[30,31] of synthesizing $CsPbX_3$ to Sb-based perovskite $Cs_3Sb_2Br_9$ NCs. We show that replacing unsaturated oleic acid (OA) with saturated octanoic acid (OnA) is critical to achieve a sufficient temperature to synthesize pure $Cs_3Sb_2Br_9$ NCs without the CsBr impurity. $Cs_3Sb_2Br_9$ NCs exhibit a 10-fold increase in performance for solar driven CO_2RR compared to Pb-based $CsPbBr_3$ NCs, producing over 500 µmol(CO)/g cat. over the course of 4 h. These experimental results are supported by density functional theory (DFT) calculations which highlight the role of crystal structure in exposing reactive surfaces on $Cs_3Sb_2Br_9$ NCs.

Synthetically, we found that pure $Cs_3Sb_2Br_9$ NCs with a single crystalline phase and uniform morphology could not be achieved using the well-established colloidal $CsPbX_3$ NCs synthetic method relying on oleic acid (OA) and oleylamine (OLA). The use of OA results in the hydrolysis of $SbBr_3$ salt[15,32] leading to the white impurity $Sb_4O_5Br_2$ (Fig 1(d), Fig S1, Fig S2). This process occurs as low as 160 °C. We found that replacing OA with OnA expanded the synthesis temperature up to 230 °C.

[a] Department of Chemistry, Wake Forest University, Winston-Salem, North Carolina 27109, USA.
[b] Center for Nanotechnology and Molecular Materials, Wake Forest University, Winston-Salem, North Carolina 27109, USA.
[c] Department of Physics, Wake Forest University, Winston-Salem, North Carolina 27109, USA.
[d] Shenzhen Engineering Lab of Flexible Transparent Conductive Films, Department of Materials Science and Engineering, Harbin Institute of Technology, Shenzhen, 518055, China.
*Email: geyersm@wfu.edu
Electronic Supplementary Information (ESI) available: [details of any supplementary information available should be included here]. See DOI: 10.1039/x0xx00000x

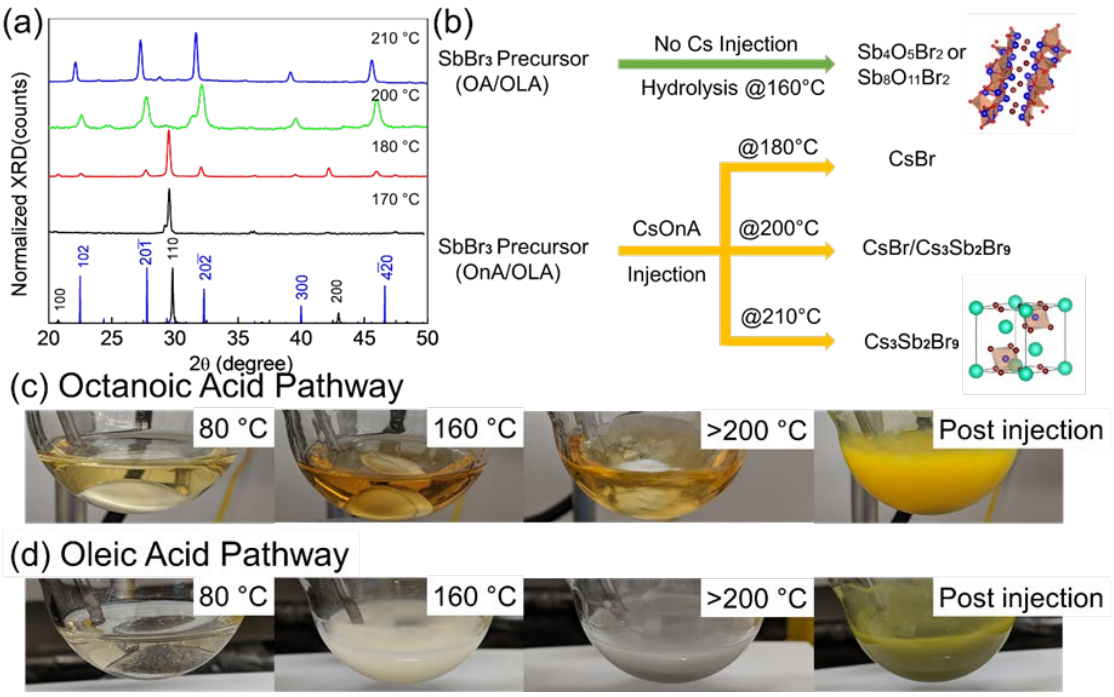

Fig 1.(a) XRD pattern for reaction products at different injection temperatures, CsBr (bottom black) and $Cs_3Sb_2Br_9$ (bottom blue, ICSD 39824); (b) Reaction scheme showing the critical role of OnA in reaching sufficient temperature for production of pure $Cs_3Sb_2Br_9$ NCs. (c)-(d) Comparison of temperature stability of OnA- and OA-based precursors.

Moreover, it suppresses the hydrolysis process (Fig 1(c)). The injection of the Cs-octanoate (CsOnA, Cs oleate equivalent in this system) at 210 °C yields high quality $Cs_3Sb_2Br_9$ NCs as shown in the X-ray diffraction pattern (Fig 1(a), Fig S3) with no CsBr impurity. In contrast, injection below 210 °C yielded high concentrations of CsBr as shown by the XRD pattern and depicted by the scheme in Fig 1(b).

The morphology of the as synthesized $Cs_3Sb_2Br_9$ NCs was imaged by scanning electronic microscopy (SEM) and transmission electronic microscopy (Fig 2(a-b). An average diameter of 37 nm is found with regular crystalline lattice (Fig S4). The inset of Fig 2(a) shows the high degree of solubility in nonpolar solvents such as hexane.

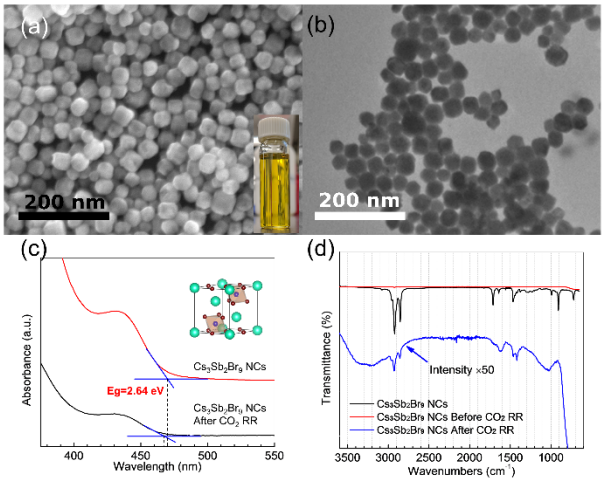

Fig 2.(a) SEM image of uniform $Cs_3Sb_2Br_9$ NCs. Inset shows yellow color and high transparency of solution; (b) TEM image of $Cs_3Sb_2Br_9$ NCs, revealing its hexagonal cubic shape. The scale bar represents 200 nm. (c) Absorption spectra of $Cs_3Sb_2Br_9$ NC before and after catalysis; (d) FTIR data for as synthesized $Cs_3Sb_2Br_9$ NCs, following ligand removal, and after catalysis. The loss of features at ~3000 cm^{-1} corresponds to the removal of the organic ligands.

Energy dispersive X-ray spectroscopy (EDS) gives a ratio of $Cs_{2.9}Sb_2Br_{7.8}$ which shows there is no excess CsBr (Fig S5). The lower than stoichiometric value for Br is likely in part due to the non-metallic nature of Br which gives an artificially low EDS value[33]. However, any Br lost from the surface is expected to strongly influence catalysis as discussed below. The TEM image reveals that the morphology of $Cs_3Sb_2Br_9$ NCs is hexagonal cubic, which is vital for the catalysis process.

The absorption onset at 470 nm in the visible region shown in Fig 2(c) corresponds to a bandgap of 2.64 eV. Prior to the CO_2RR, $Cs_3Sb_2Br_9$ NC were purified five times (see SI for details) to remove the majority of surface ligands and expose active sites. The removal of ligands is confirmed by Fourier-transform infrared spectroscopy (FTIR) (Fig 2(d)). As a result, the purified NCs have lower solubility in non-polar solvents such as hexane but are still readily dispersed as a fine powder.

For photocatalysis (details in SI), dried octadecene (ODE) was chosen as a solvent for photocatalytic CO_2RR based on its low volatility and relatively high CO_2 solubility[34] compared to alternatives such as ethyl acetate[26] or acetonitrile[28]. Purified $CsPbBr_3$ NCs were used as a reference[31]. $CsPbBr_3$ NCs produced nearly 50 µmol CO/g cat. over the course of 4 h (Fig 3(a)), slightly higher compared with previous reports[10,26,27]. This may be attributed to either the higher CO_2 concentration or reduced perovskite degradation in the ODE solvent system compared to ethyl acetate or acetonitrile. In comparison, the $Cs_3Sb_2Br_9$ NCs generated over 300 µmol CO/g cat. in the first hour, with a total

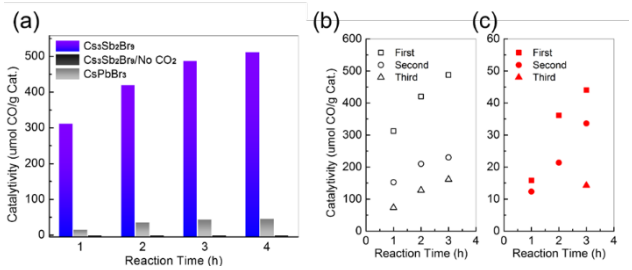

Fig 3.(a) Production of CO by $Cs_3Sb_2Br_9$ NCs, with $CsPbBr_3$ NCs as a reference; Stability test with multiple cycled reactions for (b) $Cs_3Sb_2Br_9$ NCs and (c) $CsPbBr_3$ NCs. First 2 yields in 3rd cycle for $CsPbBr_3$ too low to determine.

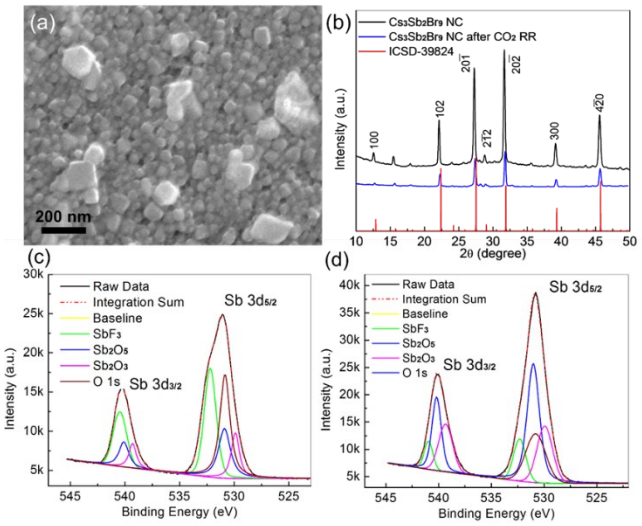

Fig 4.(a) SEM image of $Cs_3Sb_2Br_9$ NCs after catalysis; (b) XRD pattern comparison of $Cs_3Sb_2Br_9$ NCs before and after catalysis. XPS spectrum for Sb $3d_{5/2}$ electron, (c) prior and (d) after catalysis.

production of 510 µmol CO/g cat. after 4 h. This yield is over 10-fold greater than previous reports in which the halide perovskite has acted as pure catalyst[27], and even rivals the well-developed oxide perovskites (Table S6).[29] Moreover, the control experiment in which photocatalysis was run in the absence of CO_2 shows no CO production. This result indicates that CO generation is not the result of ligands or solvent decomposition. We further tested the stability of these catalysts by re-using the same catalyst for multiple reaction cycles (Fig 3(b-c)). A decrease in activity is observed, although following 9 h of testing, the $Cs_3Sb_2Br_9$ NCs are still 5 to 10-fold more active compared to the Pb-based material.

Following 4 h of CO_2RR the $Cs_3Sb_2Br_9$ NCs were collected, washed and analyzed. As shown by SEM in Fig 4(a) the morphology after catalysis exhibits aggregation. No new crystalline structures are observed in XRD (Fig 4(b)), however, the decrease in peak intensity may be due to conversion to amorphous phases. The absorption spectrum is similar in shape and onset (Fig 2(c)). The clearest change is observed by X-ray photoelectron spectroscopy (XPS) of the Sb $3d_{5/2}$ as shown in Fig 4(c-d). In the original sample, the Sb $3d_{5/2}$ is majorly comprised of a chemical state similar to SbF_3 (Fig 4(c) green curve), indicating its predominant +3 state[35,36]. This is in accord with the presence of $[SbBr_6]^{3-}$ octahedrons in the $Cs_3Sb_2Br_9$ structure (Fig S9). After the CO_2RR, the $3d_{5/2}$ peak shifts towards a binding

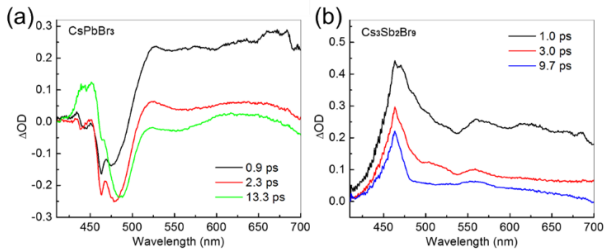

Fig 5. TA spectroscopy of (a) $CsPbBr_3$ NCs and (b) $Cs_3Sb_2Br_9$ NCs.

energy more closely corresponding to Sb_2O_5 and Sb_2O_3 (see Fig 4(d) blue and pink curve, Table S1). These results suggest that formation of an oxide with a high Sb valence[36]. Ultimately oxide formation will reduce the desirable visible light absorption, and the formation of a surface oxide may decrease catalytic activity in combination with the observed aggregation.

To better understand the remarkably different catalytic activity of $CsPbBr_3$ and $Cs_3Sb_2Br_9$, we looked at both the excited state dynamics by room temperature transient absorption (TA) spectroscopy and the reaction mechanism using density functional theory (DFT). The TA spectrum of $CsPbBr_3$ NCs shown in Fig 5(a) exhibits a negative feature at the emission wavelength indicating strong fluorescence. In contrast, the TA spectrum of $Cs_3Sb_2Br_9$ NCs shows no fluorescence feature even at very short timescales (Fig 5(b)), and a small but consistent feature at around 560 nm is observed. While further work needs to be done to understand the cause of the low fluorescence, it is notable that rapid recombination of electron and hole is not consistent with the photocatalytic activity observed. Trapping of either the hole or electron in a long-lived state could enhance the effective lifetime of the excited carriers and lead to enhanced activity, provided the electron retains sufficient energy to push forward the CO_2RR.

Density functional theory (DFT) calculations were used to find the energy of the COOH* and CO* reaction intermediates (for details see SI). For $CsPbBr_3$ NCs the (001) family of surfaces have the lowest energy, which is consistent with the cubic structure. By DFT no bound intermediate states were observed on $CsPbBr_3$ (001) which is unsurprising given that the Pb atom is completely isolated from the surface[37] by Cs and Br as depicted in Fig 6(a). In contrast, the hexagonal structure of $Cs_3Sb_2Br_9$ NCs suggests high exposure of the (0001) and (1000) surfaces. For these surfaces, the Sb atom is only partially shielded by 3 Br atoms as shown in Fig 6(c). A bound state is clearly observed for COOH* on the (1000) surface in which a single highly ionic Br is partially displaced to allow formation of the Sb-C bond. The orientation of COOH* involves some degree of stabilization via the O-Cs interaction. For CO*, the smaller size allows the Br to return to its initial position.

An analogous mechanism is observed for the $Cs_3Sb_2Br_9$ (0001) surface, again with the temporary displacement of a Br atom to form the Sb-COOH* (Fig S12). Fig 6(d) shows the calculated free-energies for each intermediate (details see Table S2). For the rate limiting step of COOH* adsorption, the COOH* intermediate has relatively high free energies of 2.25 eV for (1000) and 1.70 eV for (0001). However, compared to the completely inert $CsPbBr_3$ surface this still offers a route to

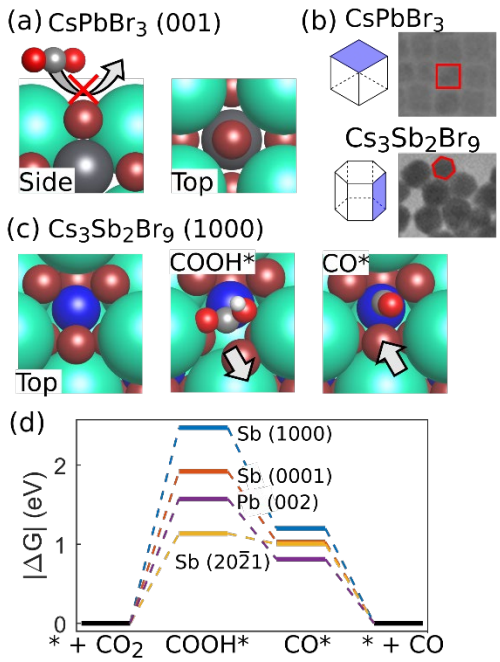

Fig 6.(a) $CsPbBr_3$ (001) surface with inaccessible Pb atoms; (b) Cubic $CsPbBr_3$ and hexagonal $Cs_3Sb_2Br_9$ NCs from TEM images, showing the planes of (001) for $CsPbBr_3$ and (1000) for $Cs_3Sb_2Br_9$; (c) Reactivity of highly exposed $Cs_3Sb_2Br_9$ (1000) surface via partial displacement of one Br. (d) Free-energy pathways for highly exposed $Cs_3Sb_2Br_9$ (1000) and (0001). Free-energies of exposed $Cs_3Sb_2Br_9$ (20$\bar{2}$1) and $CsPbBr_3$ (002) are included for comparison as models of defect site reactivity.

catalysis via plentiful sites on highly exposed surfaces. To further model the role of defect sites or high index planes in which Pb and Sb atoms are more directly exposed, the energetic pathway on the (002) plane for $CsPbBr_3$ and (20$\bar{2}$1) plane for $Cs_3Sb_2Br_9$ were calculated. For both these planes, the Pb or Sb metal center is directly accessible (Fig S12). While these high energy surfaces are not expected to be highly exposed, the fact that $CsPbBr_3$ exhibits catalytic activity despite an absence of exposed Pb on the lower energy surface suggests that defects or edge sites may play an important role in catalysis. For $Cs_3Sb_2Br_9$, Fig S12 shows that COOH* can absorb directly on Sb on the (20$\bar{2}$1) surface and a lower free energy of 0.915 eV is found. The Sb-C bond length is 2.268 Å, compared to 2.694 Å for the (1000) surface in which the Br atoms formed a partial steric barrier. Interestingly, the pathway on the $CsPbBr_3$ (002) surface has a higher free-energy for the limiting step of *COOH adsorption, suggesting that the activity of $Cs_3Sb_2Br_9$ NCs is higher for both the predominantly exposed surfaces and defect mediated catalysis.

In summary, we have developed a facile Sb-based perovskite synthesis that yields uniform distributions of highly soluble nanocrystals. The $Cs_3Sb_2Br_9$ nanocrystals show a 10-fold increase in photocatalytic CO production compared the Pb-based counterpart to achieve 510 µmol CO/g catalyst. DFT reveals viable binding sites on the (1000) and (0001) $Cs_3Sb_2Br_9$ surfaces for the key COOH* and CO* intermediates, consistent with enhanced activity compared to $CsPbBr_3$ NCs. This work shows that the limitations on stability and performance previously observed for halide-based perovskite materials can be overcome to achieve high CO_2RR activity and shows the importance of the crystal structure on determining the exposure of catalytically active surfaces in halide perovskite catalysts.

Conflicts of interest

There are no conflicts to declare.

Acknowledgements

This work was financially supported by Wake Forest University, and K.B. Ucer acknowledges support from the National Nuclear Security Administration (NNSA) Office of Defense Nuclear Nonproliferation Research and Development (DNN R&D), project LB15-V-GammaDetMater-PD2Jf, under contract AC02-05CH11231 through Lawrence Berkeley National Laboratory. C. Lu acknowledges Dr. Cynthia Day, Dr. Michael Gross and Kyle McCall for helpful discussions.

Notes and references

1 M. V. Kovalenko, L. Protesescu and M. I. Bodnarchuk, *Science*, 2017, **358**, 745–750.
2 A. Swarnkar, A. R. Marshall, E. M. Sanehira, B. D. Chernomordik, D. T. Moore, J. A. Christians, T. Chakrabarti and J. M. Luther, *Science*, 2016, **354**, 92–95.
3 X. He, Y. Qiu and S. Yang, *Adv. Mater.*, 2017, 29, 1700775.
4 H.-C. Wang, Z. Bao, H.-Y. Tsai, A.-C. Tang and R.-S. Liu, *Small*, 2018, **14**, 1702433.
5 J. Sun, J. Yang, J. I. Lee, J. H. Cho and M. S. Kang, *J. Phys. Chem. Lett.*, 2018, 1573–1583.
6 L. N. Quan, F. P. G. de Arquer, R. P. Sabatini and E. H. Sargent, *Adv. Mater.*, 2018, **30**, 1801996.
7 K. Wang, S. Wang, S. Xiao and Q. Song, *Adv. Opt. Mater.*, 2018, **6**, 1800278.
8 T. C. Jellicoe, J. M. Richter, H. F. J. Glass, M. Tabachnyk, R. Brady, S. E. Dutton, A. Rao, R. H. Friend, D. Credgington, N. C. Greenham and M. L. Böhm, *J. Am. Chem. Soc.*, 2016, **138**, 2941–2944.
9 A. Wang, Y. Guo, F. Muhammad and Z. Deng, *Chem. Mater.*, 2017, **29**, 6493-6501
10 L. Zhou, Y.-F. Xu, B.-X. Chen, D.-B. Kuang and C.-Y. Su, *Small*, 2018, 14, 1703762.
11 B. Yang, J. Chen, S. Yang, F. Hong, L. Sun, P. Han, T. Pullerits, W. Deng and K. Han, *Angew. Chem. Int. Ed.* 2018, **130**, 5457-5461.
12 Y. Bekenstein, J. C. Dahl, J. Huang, W. T. Osowiecki, J. K. Swabeck, E. M. Chan, P. Yang and A. P. Alivisatos, *Nano Lett.*, 2018, **18**, 3502-3508.
13 S. E. Creutz, E. N. Crites, M. C. De Siena and D. R. Gamelin, *Nano Lett.*, 2018, 18, 1118-1123.
14 B. Yang, F. Hong, J. Chen, Y. Tang, L. Yang, Y. Sang, X. Xia, J. Guo, H. He, S. Yang, W. Deng, K. Han, *Angew. Chem. Int. Ed.* 2019, **58**, 2278–2283.
15 B. Pradhan, G. S. Kumar, S. Sain, A. Dalui, U. K. Ghorai, S. K. Pradhan and S. Acharya, *Chem. Mater.* 2018, **30**, 2135-2142.
16 J. Pal, S. Manna, A. Mondal, S. Das, K. V. Adarsh and A. Nag, *Angew. Chem.*, 2017, **129**, 14375–14379.
17 M. Leng, Z. Chen, Y. Yang, Z. Li, K. Zeng, K. Li, G. Niu, Y. He, Q. Zhou and J. Tang, *Angew. Chem. Int. Ed.* 2016, **55**, 15012–15016.
18 B. Yang, J. Chen, F. Hong, X. Mao, K. Zheng, S. Yang, Y. Li, T. Pullerits, W. Deng and K. Han, *Angew. Chem. Int. Ed*, 2017, **56**, 12471–12475.

19 K. Ahmad, S. N. Ansari, K. Natarajan and S. M. Mobin, *ACS Appl. Energy Mater.* 2018. **1**, 2405-2409.
20 S. Liu, H. Tao, L. Zeng, Q. Liu, Z. Xu, Q. Liu and J.-L. Luo, *J. Am. Chem. Soc.*, 2017, **139**, 2160–2163.
21 J. A. Trindell, J. Clausmeyer and R. M. Crooks, *J. Am. Chem. Soc.*, 2017, **139**, 16161–16167.
22 C. M. Gabardo, A. Seifitokaldani, J. P. Edwards, C.-T. Dinh, T. Burdyny, M. G. Kibria, C. P. O'Brien, E. H. Sargent and D. Sinton, *Energy Environ. Sci.*, 2018, **11**, 2531–2539.
23 Y. Wang, D. Wang, C. J. Dares, S. L. Marquard, M. V. Sheridan and T. J. Meyer, *PNAS*, 2018, **115**, 278–283.
24 M. G. Kibria, C.-T. Dinh, A. Seifitokaldani, P. D. Luna, T. Burdyny, R. Quintero-Bermudez, M. B. Ross, O. S. Bushuyev, F. P. G. de Arquer, P. Yang, D. Sinton and E. H. Sargent, *Adv. Mater.* 2018, **30**, 1804867.
25 X. Zheng, P. De Luna, F. P. García de Arquer, B. Zhang, N. Becknell, M. B. Ross, Y. Li, M. N. Banis, Y. Li, M. Liu, O. Voznyy, C. T. Dinh, T. Zhuang, P. Stadler, Y. Cui, X. Du, P. Yang and E. H. Sargent, *Joule*, 2017, **1**, 794–805.
26 Y.-F. Xu, M.-Z. Yang, B.-X. Chen, X.-D. Wang, H.-Y. Chen, D.-B. Kuang and C.-Y. Su, *J. Am. Chem. Soc.*, 2017, **139**, 5660-5663.
27 J. Hou, S. Cao, Y. Wu, Z. Gao, F. Liang, Y. Sun, Z. Lin and L. Sun, *Chem. Eur. J.*, 2017, **23**, 9481–9485.
28 M. Ou, W. Tu, S. Yin, W. Xing, S. Wu, H. Wang, S. Wan, Q. Zhong and R. Xu, *Angew. Chem. Int. Ed.*, 2018, **57**, 13570-13574.
29 R. Shi, G. I. N. Waterhouse and T. Zhang, *Solar RRL*, 2017, **1**, 1700126.
30 L. Protesescu, S. Yakunin, M. I. Bodnarchuk, F. Krieg, R. Caputo, C. H. Hendon, R. X. Yang, A. Walsh and M. V. Kovalenko, *Nano Lett.*, 2015, **15**, 3692–3696.
31 C. Lu, M. W. Wright, X. Ma, H. Li, D. S. Itanze, J. A. Carter, C. A. Hewitt, G. L. Donati, D. L. Carroll, P. M. Lundin and S. M. Geyer, *Chem. Mater.*, 2019, **31**, 62–67.
32 J. Ota and S. K. Srivastava, *Cryst. Growth Des.*, 2007, **7**, 343–347.
33 D. E. Newbury, N. W. M. Ritchie, *Scanning* 2013, **35**, 141–168.
34 H. Nourozieh, B. Bayestehparvin, M. Kariznovi and J. Abedi, *J. Chem. Eng. Data*, 2013, **58**, 1236–1243.
35 R. Izquierdo, E. Sacher and A. Yelon, *Appl. Surf. Sci.*, 1989, **40**, 175–177.
36 F. Li, M. Xue, J. Li, X. Ma, L. Chen, X. Zhang, D. R. MacFarlane and J. Zhang, *Angew. Chem. Int. Ed.*, 2017, **56**, 14718–14722.
37 M. I. Bodnarchuk, S. C. Boehme, S. Brinck, C. Bernasconi, Y. Shynkarenko, F. Krieg, R. Widmer, B. Aeschlimann, D. Günther, M. V. Kovalenko, I. Infante, *ACS Energy Lett.* 2019. 4, 63-74

TOC Graphic Entry

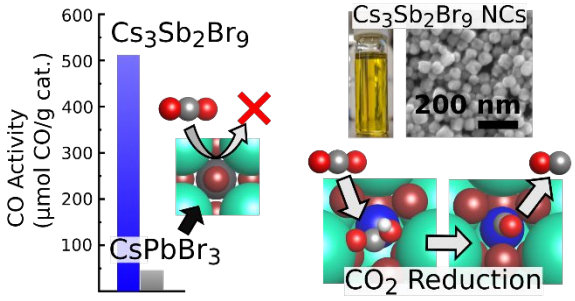

High purity synthesis yields $Cs_3Sb_2Br_9$ nanocrystals exhibiting 10-fold higher CO_2 reduction activity then $CsPbBr_3$ due to exposure of active site.